Nanoscale

PAPER

View Article Online
View Journal | View Issue

Cite this: *Nanoscale*, 2024, **16**, 16195

G_4-Hemin-loaded 2D nanosheets for combined and targeted chemo-photodynamic cancer therapy†

Gowtham Raj,[a] Tamraparni Ghosh,[a] Vasudev D. S.,[a] Harsha P.,[a] Devu B. Kumar,[b] Justin Prasad,[a] Athul V. B.,[b] Abhimanyu S. M.[b] and Reji Varghese *[a]

Synergetic combination therapy is emerging as one of the most promising approaches for cancer treatment. Among the various therapeutic approaches, PDT has received particular attention due to its non-invasive nature. However, the therapeutic performance of PDT is severely affected by tumour hypoxia. Herein, we report a supramolecular strategy for the fabrication of a PDT-active 2D nanosheet loaded with a POD mimicking DNAzyme for the synergetic combination of PDT and CDT for targeted cancer therapy. Assembly of biotin-functionalized BODIPY (**1**) and cationic β-cyclodextrin (**β-CD$^+$**) leads to the formation of a **1/β-CD$^+$** nanosheet with positively charged **β-CD$^+$** on the surface of the sheet. The cationic face of the **1/β-CD$^+$** sheet was then loaded with a POD-mimicking **Hem**-loaded G-quadruplex aptamer (**Hem/DNA1**) *via* electrostatic interactions (**1/β-CD$^+$/Hem/DNA1**). Cellular internalization of the **1/β-CD$^+$/Hem/DNA1** nanosheet occurs *via* a receptor-mediated endocytic pathway, which then undergoes lysosomal escape. Subsequently, **Hem/DNA1** on the surface of **1/β-CD$^+$/Hem/DNA1** reacts with endogenous H_2O_2 *via* the Fenton pathway to produce $^{\bullet}OH$ and O_2. Moreover, under cellular conditions, **Hem** inside the **1/β-CD$^+$/Hem/DNA1** nanosheet produces Fe^{2+}, which then undergoes another Fenton reaction to produce $^{\bullet}OH$ and O_2. The Fe^{3+} generated after the Fenton reaction is then reduced *in situ* to Fe^{2+} by glutathione for the next Fenton cycle. At the same time, photoirradiation of the **1/β-CD$^+$** nanosheet using a 635 nm laser produces $^1O_2$ *via* the PDT pathway by using endogenous O_2. The most remarkable feature of the present nanoformulation is the cooperativity in its therapeutic action, wherein O_2 produced during the CDT pathway was used by the **1/β-CD$^+$** sheet for improving its PDT efficacy in the hypoxic tumor microenvironment. This work represents a unique combination of CDT and PDT for targeted cancer therapy, wherein the CDT action of the nanoagent enhances the PDT efficacy and we strongly believe that this approach would encourage researchers to design similar combination therapy for advancements in the treatment of cancer.

Received 5th April 2024,
Accepted 28th July 2024

DOI: 10.1039/d4nr01494d

rsc.li/nanoscale

Introduction

Photodynamic therapy (PDT) is a promising treatment modality for cancer mainly due to its non-invasive nature and spatiotemporal controllability.[1,2] It involves the photoexcitation of a photosensitizer, preferably in the near-infrared (NIR) region, which then undergoes intersystem crossing from the singlet excited state to the triplet excited state. The triplet state of the sensitizer then acts as an energy donor to the ground state of molecular oxygen ($^3O_2$) and other molecules present in the tissue, producing highly cytotoxic reactive oxygen species (ROS) including singlet oxygen ($^1O_2$). These reactions lead to cell death in the photoirradiated region.[3–9] Although considerable advancement has been made in PDT-based cancer treatment, the condition of hypoxia (reduced oxygen concentration) in solid tumours significantly reduces the efficiency of PDT for cancer treatment.[10,11] Different strategies have been developed in recent years to overcome the condition of tumour hypoxia such as transporting additional O_2 to the tumor microenvironment[12,13] and catalysing endogenous H_2O_2 to O_2.[14,15] Though these strategies showed an enhanced supply of O_2 to the hypoxic tumours to some extent, the continuous consumption of O_2 by the mitochondria for the synthesis of ATP significantly hinders the efficacy of these

[a]*School of Chemistry, Indian Institute of Science Education and Research (IISER) Thiruvananthapuram, Trivandrum-695551, Kerala, India.*
E-mail: reji@iisertvm.ac.in
[b]*School of Biology, Indian Institute of Science Education and Research (IISER) Thiruvananthapuram, Trivandrum-695551, Kerala, India*

† Electronic supplementary information (ESI) available. See DOI: https://doi.org/10.1039/d4nr01494d

approaches. Therefore, development of new strategies to boost O_2 concentration in hypoxic tumours is extremely important for PDT-based cancer therapy.[16–18]

Chemodynamic therapy (CDT) is another potential therapeutic approach for cancer treatment and has shown significant growth in recent years.[19,20] This involves the metal-catalysed conversion of endogenous H_2O_2 into highly reactive hydroxyl radicals ($^{\bullet}OH$) *via* a Fenton or Fenton-like reaction.[21,22] It is important to note that one of the by-products of the Fenton reaction is O_2. This clearly suggests that the integration of a CDT agent into the PDT system would be a promising approach for the improvement of PDT action by boosting the concentration of O_2. More importantly, CDT and PDT can work in a synergetic fashion wherein O_2 generated using the Fenton reaction can enhance the PDT action and at the same time $^{\bullet}OH$ generated *via* the Fenton reaction is toxic to the cancer cells. Hence, this strategy offer the design of a synergetic combination of PDT and CDT for the treatment of cancer.[23–28]

We have recently reported a fluorinated boron-dipyrromethene (BODIPY)-based nanosheet as a nanoformulation for combined antisense DNA delivery and PDT.[29] The nanosheet exhibited a high extinction coefficient in the NIR region, excellent $^1O_2$ generation upon photoirradiation and efficient delivery of antisense DNA.[30,31] Because the surface of the nanosheet is cationic in nature, it permits the integration of any functional DNA onto its surface *via* electrostatic interactions. In view of this, we envisioned that the incorporation of a peroxidase (POD)-mimicking DNAzyme[32–35] onto PDT-active nanosheets would be a promising nanoformulation to achieve the design of a synergetic combination of CDT and PDT.[36–38] For example, G-rich DNA is known to fold G-quadruplexes that show high binding affinity to hemin (**Hem**) to form a **Hem**-bound G-quadruplex, which is known to exhibit POD activity to produce $^{\bullet}OH$ and O_2.[39] In addition, the G-quadruplex can function as an aptamer for specific cancer cells and hence offer targeted delivery of therapeutic agents into cancerous cells.[40,41]

Herein, we report a supramolecular strategy for the fabrication of a PDT-active 2D nanosheet loaded with a POD-mimicking DNAzyme for synergetic combination of PDT and CDT for cancer therapy. As reported previously, the host–guest interaction between biotin-functionalized BODIPY (**1**) and cationic β-cyclodextrin (**β-CD$^+$**) in aqueous medium resulted in the formation of a **1/β-CD$^+$** nanosheet with positively charged **β-CD$^+$** exposed onto the surface of the sheet.[29] The cationic faces of **1/β-CD$^+$** were then loaded with a POD-mimicking **Hem**-loaded G-quadruplex aptamer (**Hem/DNA1**) *via* electrostatic interactions to form a **1/β-CD$^+$/Hem/DNA1** nanosheet. Importantly, **DNA1** (DNAzyme) on the surface of the nanosheet can act as a targeting ligand for the overexpressed nucleolin protein on the surface of cancer cells (*e.g.*: MDA-MB-231) for the selective delivery of PDT and CDT agents.[42–44] After selective cellular internalization of the **1/β-CD$^+$/Hem/DNA1** nanosheet *via* the receptor-mediated endocytic pathway, it undergoes lysosomal escape due to the cationic charge on the surface of the nanosheet, which potentially prevents its degradation in the lysosome. Subsequently, **Hem/DNA1** on the surface of **1/β-CD$^+$/Hem/DNA1** reacts with endogenous H_2O_2 *via* the Fenton pathway to produce $^{\bullet}OH$ and O_2. Moreover, under cellular conditions, over time, **Hem** inside the **1/β-CD$^+$/Hem/DNA1** nanosheet produces Fe^{2+} by the enzymatic action of intracellular heme oxygenase.[45] The *in situ* generated Fe^{2+} then undergoes another Fenton reaction to produce $^{\bullet}OH$ and O_2. The Fe^{3+} generated after the Fenton reaction is then reduced *in situ* to Fe^{2+} by glutathione (GSH) for the next Fenton cycle. At the same time, photoirradiation of the **1/β-CD$^+$** nanosheet using a 635 nm laser produces $^1O_2$ *via* PDT by using endogenous O_2. The most remarkable feature of the nanoformulation is the cooperativity in its therapeutic action, wherein O_2 produced during the CDT pathway was used by the **1/β-CD$^+$** sheet for improving its PDT efficacy in the hypoxic tumor microenvironment (Scheme 1).

Results and discussion

Initially, PDT (**1/β-CD$^+$**) and CDT (**Hem/DNA1**) agents were synthesized independently. Syntheses of **β-CD$^+$** and **1** were achieved as per previously reported procedures.[46–48] Non-covalent synthesis of the **1/β-CD$^+$** supramolecular amphiphile was achieved by annealing **β-CD$^+$** (20 μM in water) and **1** (20 μM in DMSO) at 90 °C for 5 minutes, followed by slow cooling to room temperature, as reported earlier.[29] Unassembled **β-CD$^+$** and **1** present in the solution were removed by repeated centrifugation (3 times at 3000 rpm for 5 minutes), and the supernatant obtained was used for further experiments. It was earlier reported by us that the **1/β-CD$^+$** amphiphile spontaneously self-assembled into a 2D nanosheet with lateral dimensions in the range of several hundred nm to μm with the thickness of the sheet in the range of 6–10 nm (Fig. S1†).[29] Similarly, a **Hem/DNA1** DNAzyme was synthesized by annealing **DNA1** (5′-GGTGGTGGTGGTTGGGTGGTGGTG GAAAAAAAAA-3′) (1 μM) and **Hem** (1 μM) in Tris EDTA KCl buffer (pH 7) at 60 °C, followed by slow cooling to room temperature. The solution was then subjected to centrifugal cut-off filtration to remove any unbound **Hem**. In the presence of K^+, the G-rich oligonucleotide undergoes intramolecular folding to form a G-quadruplex, which facilitates the end stacking of **Hem** to form a **Hem/DNA1** DNAzyme.[39] The circular dichroism (CD) spectrum of **Hem/DNA1** revealed the characteristic spectral features of the antiparallel G-quadruplex (Fig. 1a).[49] Furthermore, no change in the CD spectrum was observed even after the end stacking of **Hem** on the G-quadruplex, implying its structural stability. The loading of **Hem** onto **DNA1** was confirmed by absorption spectral studies. A broad absorption spectrum was observed for **Hem** (1 μM) in water due to its very poor water solubility and hence **Hem** exists as an aggregated species in water, whereas intense and sharp absorption bands were observed for **Hem** in DMSO, implying that **Hem** exists as monomeric species in DMSO. Interestingly, monomer-like absorption spectral features with intense and

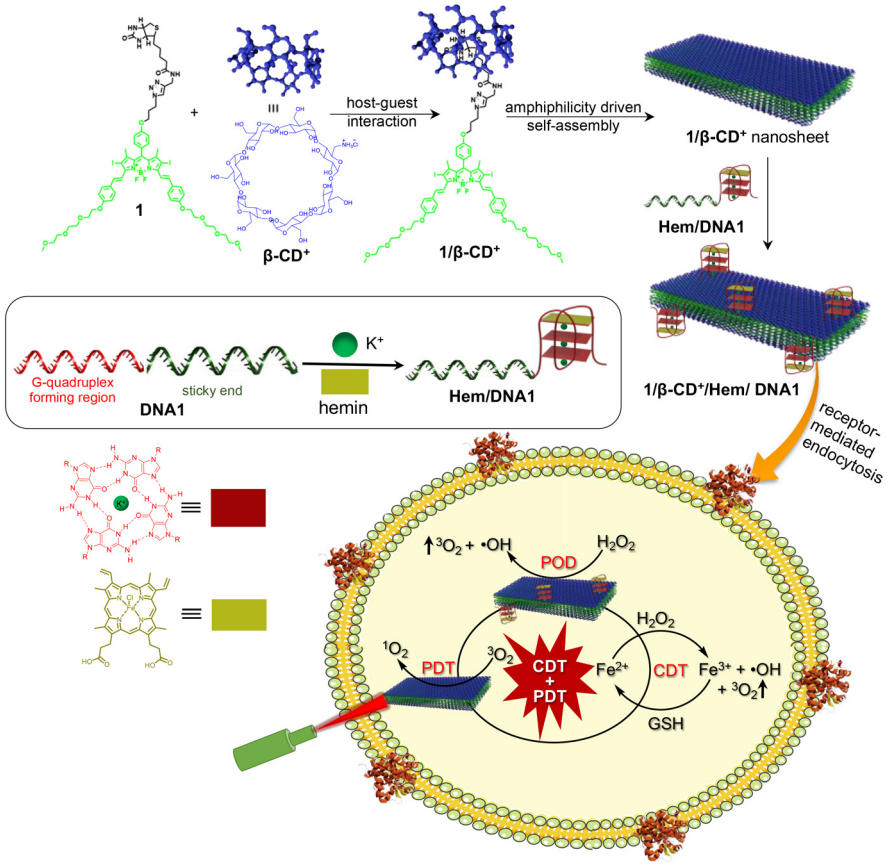

Scheme 1 Scheme showing the non-covalent synthesis of the **1/β-CD$^+$** complex and its spontaneous self-assembly for the formation of a **1/β-CD$^+$** nanosheet. Integration of **Hem/DNA1** onto the surface of the **1/β-CD$^+$** nanosheet *via* electrostatic interactions is also shown. Cellular internalization of **1/β-CD$^+$/Hem/DNA1** into MDA-MB-231 cells through receptor mediated endocytosis and the mechanism of combined PDT and CDT are also demonstrated.

sharp absorption bands were observed for **Hem** in water in the case of **Hem/DNA1** (1/1 μM, Fig. 1b). This must be due to the end stacking of **Hem** on the **DNA1** G-quadruplex, which prevents its aggregation in water.

We then evaluated the POD-mimicking activity of **Hem/DNA1** by using the tetramethylbenzidine (TMB) oxidation assay (Fig. 1c). For this, **Hem/DNA1** (1/1 μM) was treated with TMB (200 μM) in the presence of H_2O_2 (200 μM) and the emergence of the peak corresponding to oxidized TMB at 650 nm was monitored. As expected, a strong peak at 650 nm was observed for the **Hem/DNA1**-treated sample demonstrating its excellent catalytic activity. On the other hand, only negligible activity was observed for free **Hem**. Subsequently, **Hem/DNA1** was loaded onto the surface of the **1/β-CD$^+$** sheet by annealing **Hem/DNA1** (1/1 μM) and **1/β-CD$^+$** (20/20 μM) at 40 °C for 10 minutes, followed by slow cooling to room temperature to yield **1/β-CD$^+$/Hem/DNA1**. The loading efficiency of **Hem/DNA1** onto the surface of the **1/β-CD$^+$** nanosheet was found to be ~100%. Details of the calculation of the loading efficiency are provided in the ESI (Fig. S2†). Zeta potential analyses of **Hem/DNA1** and **1/β-CD$^+$** showed values of −24.2 and +15.27 mV, respectively (Fig. 1d), whereas **1/β-CD$^+$/Hem/DNA1** showed a zeta potential value of +7.9 mV. This significant reduction in the zeta potential value for **1/β-CD$^+$/Hem/DNA1** (+7.9 mV) compared to that of the **1/β-CD$^+$** sheet (+15.27 mV) can be attributed to the successful loading of negatively charged **Hem/DNA1** onto the cationic surface of the **1/β-CD$^+$** sheet *via* electrostatic interactions. Interestingly, the sheet morphology of **1/β-CD$^+$** was found to remain intact even after the loading of **Hem/DNA1** as evident from the transmission electron microscopy (TEM) (Fig. 1e) and atomic force microscopy (AFM) (Fig. 1f) analyses. The nanosheet morphology of **1/β-CD$^+$/Hem/DNA1** was further confirmed by confocal laser scanning microscopy (CLSM) analyses using **DNA1** labelled with FAM (**DNA2**), which showed the formation of green fluorescent 2D nanosheets (Fig. 1g). Furthermore, the **1/β-CD$^+$/Hem/DNA1** nanosheet was found to be structurally stable in PBS buffer and 10% serum at pH 7.0. This was evident from the time-dependent absorption spectral changes of the **1/β-CD$^+$/Hem/DNA1** nanosheet, which revealed no change in the characteristic absorption of the nanosheet with respect to time, at least for up to 6 h (Fig. S3†). We also evaluated whether the POD-mimicking activity of **Hem/DNA1** is maintained after loading onto the nanosheet. As expected, a strong absorption peak at 650 nm was observed for **1/β-CD$^+$/Hem/DNA1**-treated samples, validating its catalytic activity even after loading onto the nanosheet (Fig. 1c).

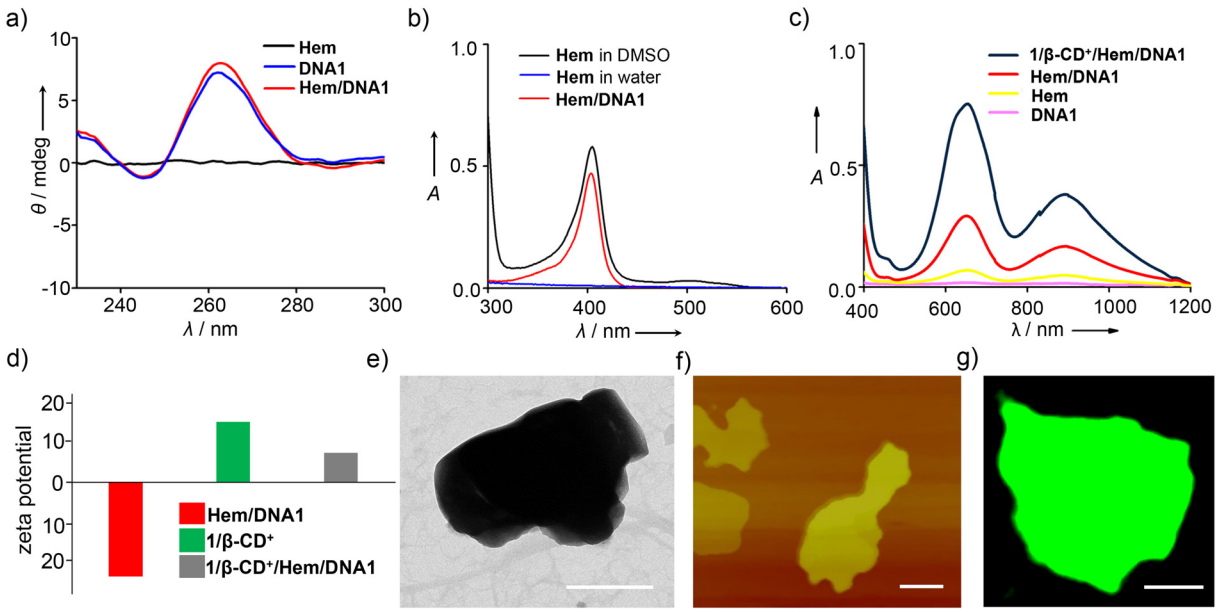

Fig. 1 (a) Comparison of the CD spectra of **DNA1**, **Hem**, and **Hem/DNA1**. (b) Comparison of the absorption spectra of **Hem** (in H_2O and DMSO) and **Hem/DNA1**. (c) Comparison of the absorption spectra of TMB-treated solutions of **DNA1**, **Hem**, **Hem/DNA1** and **1/β-CD$^+$/Hem/DNA1**. (d) Comparison of the zeta potentials of **Hem/DNA1**, **1/β-CD$^+$** and **1/β-CD$^+$/Hem/DNA1**. (e) TEM and (f) AFM images of **1/β-CD$^+$/Hem/DNA1** (scale bars represent 500 nm). (g) CLSM image of **1/β-CD$^+$/Hem/DNA2** (**DNA2** is FAM-labelled **DNA1**) (scale bar represents 5 μm).

One of the by-products of the CDT action of **Hem/DNA1** is O_2 and hence the *in situ* generated O_2 can be utilized by the photosensitizer (**1/β-CD$^+$**) for the enhanced generation of $^1O_2$ under hypoxic conditions of the tumour microenvironment. The CDT-assisted enhanced PDT of **1/β-CD$^+$/Hem/DNA1** was studied using the 1,3-diphenylisobenzofuran (DPBF) degradation assay. For this, **Hem/DNA1** (1/1 μM) and **1/β-CD$^+$/Hem/DNA1** (50/50/1/1 μM) nanosheet solutions in water (pH 6.5) containing H_2O_2 (200 μM) and DPBF (200 μM) were irradiated with a 635 nm laser (0.75 W cm^{-2}) for 70 s and the decrease in the absorption band of DPBF at 420 nm was monitored with respect to time (Fig. 2). The absorption spectrum of DPBF was considered as the control (100%) and no degradation was observed in this case. A decrease in DPBF absorption of 27% was observed for the **Hem/DNA1**-treated sample compared to DPBF alone, indicating the degradation of DPBF by the $^{\bullet}$•OH *in situ* generated by the CDT action of **Hem/DNA1**. Interestingly, a drastic decrease in DPBF absorption of 73% was observed for the **1/β-CD$^+$/Hem/DNA1**-treated sample. This enhanced degradation of DPBF in the case of **1/β-CD$^+$/Hem/DNA1** compared to **Hem/DNA1** must be attributed to the synergetic action of CDT and PDT, wherein O_2 generated during the CDT action of **Hem/DNA1** enhances the PDT action of **1/β-CD$^+$**.

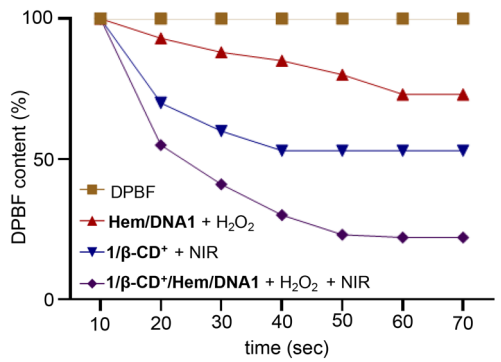

Fig. 2 Plot of absorbance changes of DPBF at 420 nm of DPBF-treated solutions of **Hem/DNA1**, **1/β-CD$^+$** and **1/β-CD$^+$/Hem/DNA1** under photoirradiation with a 635 nm laser for 70 s (0.75 W cm^{-2}).

Having demonstrated the synergetic action of CDT and PDT, the therapeutic performance of the **1/β-CD$^+$/Hem/DNA1** nanosheet for combined CDT and PDT-based cancer therapy was studied using triple-negative human breast cancer cells, MDA-MB-231, as a representative cell line. Initially, the cellular internalization of **1/β-CD$^+$/Hem/DNA2** (20/20/1/1 μM) was investigated using CLSM analyses by monitoring the green fluorescence of **DNA2**. After 12 h of incubation, CLSM analyses revealed strong green fluorescence for the cells that was mainly distributed through the cytosolic regions of the cells (Fig. 3a and b). This indicates the efficient internalization of **1/β-CD$^+$/Hem/DNA2** into MDA-MB-231 cells. It is important to note that **Hem/DNA1** acts not only as a CDT agent, but also as a targeting ligand for MDA-MB-231 cells. Targeting cancer cells is due to the molecular recognition of nucleolin protein overexpressed on the surface of MDA-MB-231 cells by **Hem/DNA2**. Therefore, **Hem/DNA2** preferably permits the selective internalization of the nanoformulation into the cancer cells compared to the normal healthy cell lines. The selective internalization of **1/β-CD$^+$/Hem/DNA2** was evaluated by com-

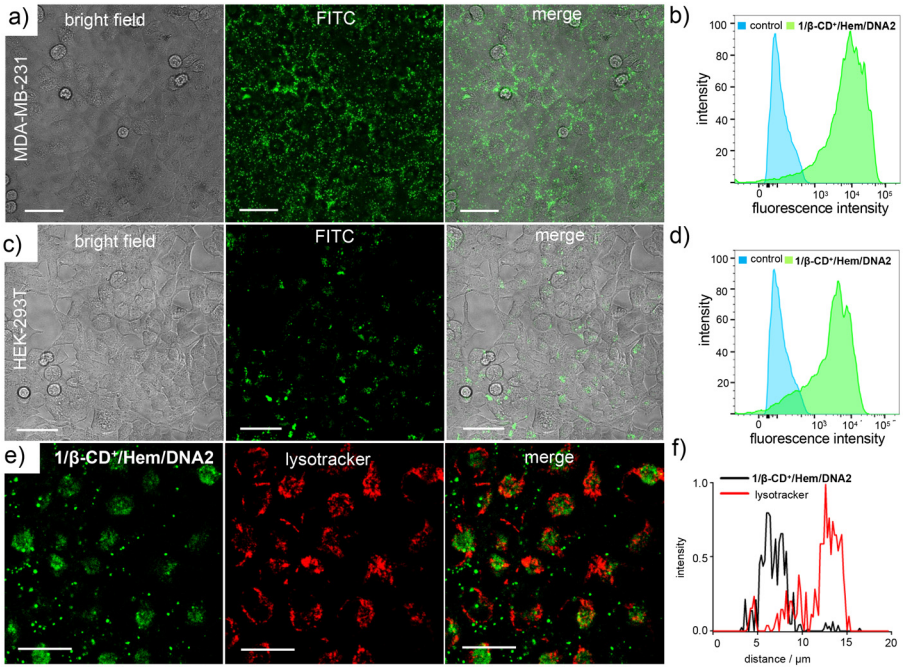

Fig. 3 (a) CLSM images of **1/β-CD$^+$/Hem/DNA2**-treated MDA-MB-231 cells (scale bar represents 50 μm) and (b) the corresponding FACS analyses. (c) CLSM images of **1/β-CD$^+$/Hem/DNA2**-treated HEK-293T cells (scale bar represents 50 μm) and (d) the corresponding FACS analyses. (e) CLSM images of **1/β-CD$^+$/Hem/DNA2**-treated MDA-MB-231 cells stained with LysoTracker Red (scale bar represents 25 μm) and (f) the corresponding line analyses.

paring its cellular internalization between HEK-293T (normal cell line), which has negligible expression of nucleolin on its surface, and MDA-MB-231 cancer cells (Fig. 3a–d). In accordance with our design, CLSM analyses clearly showed strong green fluorescence for **1/β-CD$^+$/Hem/DNA2**-treated MDA-MB-231 cells (Fig. 3a and b) when compared to the corresponding HEK-293T cells (Fig. 3c and d). In support of this, fluorescence-activated cell sorting (FACS) analyses revealed a high mean fluorescence intensity (MFI) shift for MDA-MB-231 (11 490) compared to HEK-293T cells (4440).

Typically any foreign materials entering into a cell *via* the endocytic pathway ultimately reach the lysosome and becomes degraded in the lysosome due to its acidic pH. In order to check whether the nanosheet reaches the lysosome after its cellular internalization, colocalization studies were performed after staining the lysosome of the cells using LysoTracker Red (Fig. 3e). As is evident from the CLSM analyses, only very poor colocalization was observed for the **1/β-CD$^+$/Hem/DNA2** nanosheet with LysoTracker Deep Red. This suggests that the **1/β-CD$^+$/Hem/DNA2** nanosheet undergoes lysosomal escape immediately after receptor-mediated endocytosis and escapes degradation in the lysosome. This was further supported by the corresponding line analyses, which showed a relatively low Pearson coefficient value of 0.048 (Fig. 3f). We believe that the lysosomal escape of the **1/β-CD$^+$/Hem/DNA2** nanosheet is due to the net positive charges present on the surface of the nanosheet, which favours lysosomal membrane destabilization, as reported previously by our own group and others.[50] The lysosomal escape of **1/β-CD$^+$/Hem/DNA2** prevents the degradation of the nanosheet at the acidic lysosomes, thereby improving the efficacy of the nanoformulation.

After establishing the escape of the **1/β-CD$^+$/Hem/DNA2** nanosheet from the lysosomes, the ROS generation efficiency of the **1/β-CD$^+$/Hem/DNA1** nanosheet inside MDA-MB-231 cells was investigated using 2′,7′-dichlorofluorescein diacetate (DCFH-DA) as a fluorescent probe for ROSs. For this, MDA-MB-231 cells were treated with **Hem/DNA1**, **1/β-CD$^+$/Hem/DNA1**, **1/β-CD$^+$** + NIR or **1/β-CD$^+$/Hem/DNA1** + NIR (635 nm laser with a power of 0.75 W cm^{-2} for 10 minutes) and *in situ* ROS generation inside the cell was monitored using the DCFH-DA assay, which produces fluorescent green 2,7-dichlorofluorescein (DCF) upon ROS detection (Fig. 4a). CLSM analyses clearly revealed that the maximum green fluorescence intensity of DCF was associated with **1/β-CD$^+$/Hem/DNA1** + NIR-treated cells compared to **Hem/DNA1**, **1/β-CD$^+$/Hem/DNA1**, and **1/β-CD$^+$** + NIR-treated cells. These results unequivocally confirm that **1/β-CD$^+$/Hem/DNA1** + NIR-treated cells produce maximum ROSs inside the cells upon laser irradiation and this must be attributed to the synergetic action of CDT and PDT. In accordance with the CLSM analysis, FACS analyses disclosed MFI shift values of 6052, 1240, 463 and 127 for **1/β-CD$^+$/Hem/DNA1** + NIR, **1/β-CD$^+$**, **Hem/DNA1** and untreated MDA-MB-231 cells, respectively (Fig. S5†). A maximum MFI shift was observed for **1/β-CD$^+$/Hem/DNA** + NIR-treated cells. As expected, no significant ROS generation was observed for **1/β-CD$^+$/Hem/DNA**-treated cells in the absence of photoirradiation.

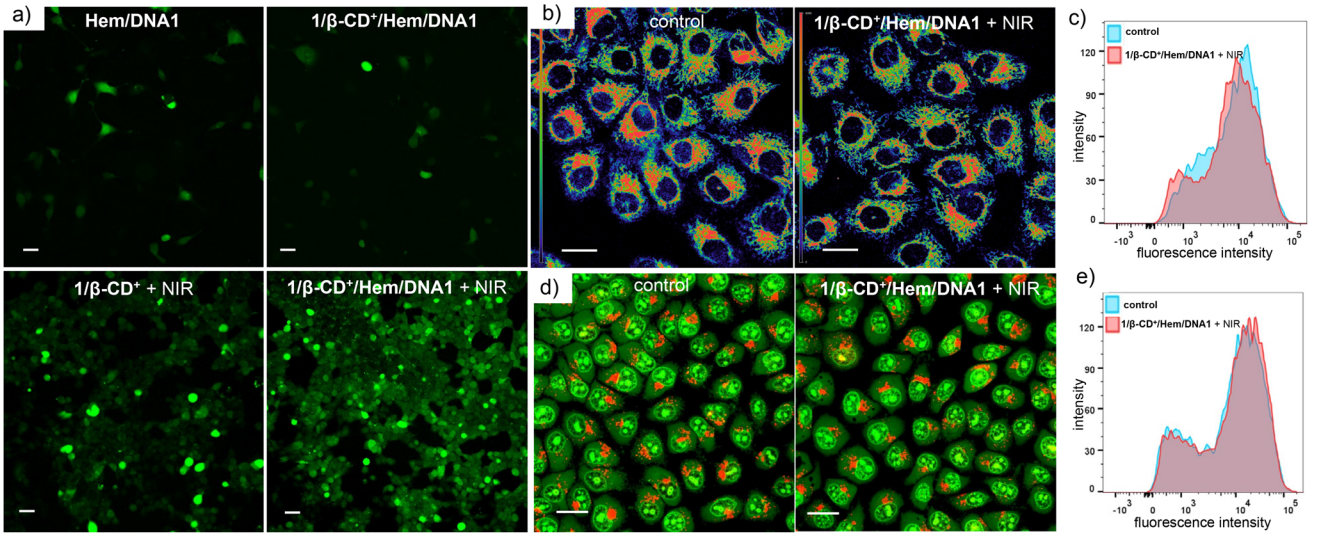

Fig. 4 (a) DCFH-DA assay: CLSM images of **Hem/DNA1**, **1/β-CD$^+$/Hem/DNA1**, **1/β-CD$^+$** + NIR and **1/β-CD$^+$/Hem/DNA1** + NIR-treated MDA-MB-231 cells (635 nm laser with a power of 0.75 W cm^{-2}) (scale bar represents 25 μm). (b) TMRM assay: CLSM images of **1/β-CD$^+$/Hem/DNA1**-treated MDA-MB-231 cells stained with TMRM under photoirradiation with a 635 nm laser (0.75 W cm^{-2}) (scale bar represents 25 μm) and (c) the corresponding FACS analyses. (d) AO assay: CLSM images of **1/β-CD$^+$/Hem/DNA1**-treated MDA-MB-231 cells stained with AO under photoirradiation with a 635 nm laser (0.75 W cm^{-2}) (scale bar represents 25 μm) and (e) the corresponding FACS analyses.

Because ROSs such as $^1O_2$ and $^{\bullet}OH$ are highly oxidizing in nature, they can induce damage to organelles like lysosomes and mitochondria, which can potentially lead to apoptosis by various signalling pathways. In view of this, we examined the structural integrity of these organelles in the presence of ROSs generated by the combined CDT and PDT. The mitochondrial damage caused by the ROSs was evaluated using the tetramethylrhodamine methyl ester perchlorate (TMRM) assay (Fig. 4b and c).[51] Since mitochondria have typical membrane potentials in the range of −180 mV, they can accumulate high concentrations of cationic dyes like TMRM. If mitochondria are damaged or depolarized, dye accumulation gradually decreases, which leads to a diminishing of its fluorescence intensity. For this, MDA-MB-231 cells were treated with **1/β-CD$^+$/Hem/DNA1** (20/20/1/1 μM) for 2 h, then kept under NIR light illumination (635 nm laser at 0.75 W cm^{-2}) for 10 minutes followed by 3 h of incubation. The cells were then stained with TMRM, and changes in the green fluorescence intensity of TMRM were probed using CLSM analyses. In this case as well, CLSM analyses of **1/β-CD$^+$/Hem/DNA1**-treated MDA-MB-231 cells showed no decrease in the fluorescence intensity when compared to the corresponding control cells, indicating the healthy nature of the mitochondria (Fig. 4b). This was further quantified by FACS analyses (Fig. 4c), which disclosed similar MFI shift values for the **1/β-CD$^+$/Hem/DNA1**-treated cells (12 674) and the corresponding untreated control cells (12 660). The lysosomal integrity was further evaluated using an acridine orange (AO) assay (Fig. 4d and e).[52,53] Acridine orange emits green fluorescence when bound to dsDNA in the nucleus and red fluorescence inside lysosomes. If the lysosome is damaged, it leads to a decrease in the red fluorescence of AO. For this purpose, MDA-MB-231 cells were treated with **1/β-CD$^+$/Hem/DNA1** (20/20/1/1 μM) for 2 h followed by NIR light illumination for 10 minutes followed by 3 h of incubation. Subsequently, the cells were co-stained with AO and evaluated using CLSM analyses. The CLSM images of **1/β-CD$^+$/Hem/DNA1**-treated cells showed no noticeable decrease in the red fluorescence of AO with respect to the control cells, indicating that the lysosomes were not damaged by the ROSs generated by the **1/β-CD$^+$/Hem/DNA1** nanosheet (Fig. 4d). This was further confirmed by FACS analyses, which showed MFI shift values of 16 476 and 17 527 for the control and **1/β-CD$^+$/Hem/DNA1** nanosheet-treated MDA-MB-231 cells, respectively (Fig. 4e). However, it must be noted that TMRM and AO staining assays revealed significant damage to lysosomes and mitochondria after 24 h of incubation (Fig. S6†). These results indicate that ROSs cause damage to the cell organelles over longer time-scales of incubation, but remain intact during shorter incubation times.

After demonstrating selective internalization and ROS generation inside the cancer cells, the cytotoxicity of **1/β-CD$^+$/Hem/DNA1** towards MDA-MB-231 cells was studied using the MTT assay.[54] Initially, toxicities of **β-CD$^+$** and **1/β-CD$^+$** nanosheets towards MDA-MB-231 cells in the dark were studied (Fig. 5a and b). For this, **β-CD$^+$** (Fig. 5a) and **1/β-CD$^+$** (Fig. 5b) nanosheets of varying concentrations (1–20 μM) in the dark were treated with MDA-MB-231 cells for 24 h. As expected, no cytotoxicity was observed even at the higher concentration of 20 μM. Subsequently, the cytotoxicities of MDA-MB-231 cells treated with **Hem/DNA1** (1/1 μM), **1/β-CD$^+$/Hem/DNA1** (20/20/1/1 μM), **1/β-CD$^+$** (20/20 μM) + NIR, and **1/β-CD$^+$/Hem/DNA1** + NIR (20/20/1/1 μM) for 2 h (635 nm laser with a power of 0.75 W cm^{-2} for 10 minutes) were studied (Fig. 5c). As expected no significant cytotoxicity was observed for **Hem/DNA1** and

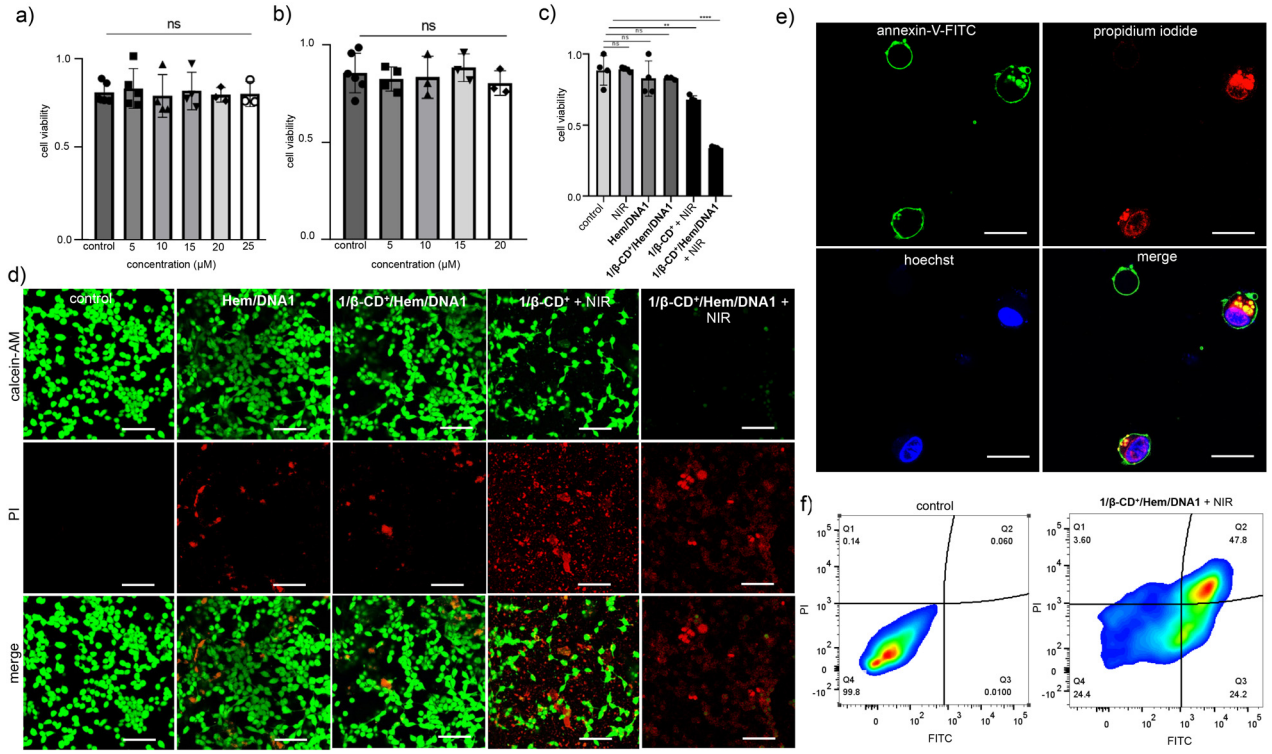

Fig. 5 (a)–(c) MTT assay: cell viability at varying concentrations of (a) **β-CD$^+$** and (b) **1/β-CD$^+$**-treated MDA-MB-231 cells in the dark. (c) MTT assay of **Hem/DNA1**, **1/β-CD$^+$/Hem/DNA1**, **1/β-CD$^+$** + NIR and **1/β-CD$^+$/Hem/DNA1** + NIR-treated MDA-MB-231 cells (635 nm laser with a power of 0.75 W cm^{-2}). (d) Calcein-AM/PI live–dead assay: CLSM images of **Hem/DNA1**, **1/β-CD$^+$/Hem/DNA1**, **1/β-CD$^+$** + NIR and **1/β-CD$^+$/Hem/DNA1** + NIR-treated MDA-MB-231 cells (scale bar represents 100 μm). (e) Annexin V-FITC/PI assay: CLSM images of **1/β-CD$^+$/Hem/DNA1**-treated MDA-MB-231 cells under photoirradiation using a 635 nm laser (0.75 W cm^{-2}) (scale bar represents 25 μm) and (f) the corresponding FACS analyses.

1/β-CD$^+$/Hem/DNA1 in the absence of NIR light, indicating the poor therapeutic efficacy. On the other hand, significant cytotoxicity was observed for **1/β-CD$^+$** and **1/β-CD$^+$/Hem/DNA1**-treated cells under NIR light irradiation. Interestingly, enhanced cytotoxicity was observed for **1/β-CD$^+$/Hem/DNA1**-treated cells compared to **1/β-CD$^+$**-treated cells. A cell death extent of 65% was observed for **1/β-CD$^+$/Hem/DNA1**-treated cells, whereas only 32% cell death was observed for **1/β-CD$^+$**-treated cells. These results are in full agreement with the enhanced ROS generation for **1/β-CD$^+$/Hem/DNA1**-treated cells and fully support our hypothesis of synergetic CDT and PDT actions.

To further support the cytotoxicity induced by the combined actions of CDT and PDT by the **1/β-CD$^+$/Hem/DNA1** nanosheet towards MDA-MB-231 cells, the calcein-AM/PI co-staining assay was performed (live/dead assay) (Fig. 5d). Calcein-AM interacts with the esterase present inside live cancer cells and produces green fluorescence from the cells due to the cleavage of the acetoxymethyl (AM) ester-protecting group of calcein-AM. On the other hand, no ester cleavage is possible inside the dead cells as the concentration of esterase is very minimal and hence no green fluorescence is expected for the dead cells. Similarly, propidium iodide (PI) cannot pass through the cell membrane of live cells, whereas it can stain the dead cell to give red fluorescence.[43] To demonstrate the live/dead assay, the cells were initially treated with **Hem/DNA1**, **1/β-CD$^+$/Hem/DNA1**, **1/β-CD$^+$** + NIR, and **1/β-CD$^+$/Hem/DNA1** + NIR for 2 h (635 nm laser with a power of 0.75 W cm^{-2} for 10 minutes). As shown in Fig. 5d, **1/β-CD$^+$/Hem/DNA1** + NIR-treated cells exhibited mainly red fluorescence of PI and negligible green fluorescence of calcein-AM compared to **Hem/DNA1**, **1/β-CD$^+$/Hem/DNA1**, and **1/β-CD$^+$** + NIR-treated cells. These results conclude the enhanced cytotoxicity of **1/β-CD$^+$/Hem/DNA1** + NIR compared to **1/β-CD$^+$** + NIR, **Hem/DNA1** and **1/β-CD$^+$/Hem/DNA1**. The live/dead cell assay also supports our hypothesis of enhanced cytotoxicity for **1/β-CD$^+$/Hem/DNA1** + NIR due to the synergetic combination of CDT and PDT.

In order to understand the cell death mechanism of the present nanoformulation, the Annexin V-FITC(AV)/PI staining assay was carried out on **1/β-CD$^+$/Hem/DNA1**-treated MDA-MB-231 cells under NIR light illumination. As shown in Fig. 5e and Fig. S7,† **1/β-CD$^+$/Hem/DNA1** (20/20/1/1 μM)-treated cells exhibited the intense green fluorescence of Annexin V-FITC around the cell membrane and the strong red fluorescence of PI from the nuclei, revealing that most of the cell population is in the late stage of the apoptotic pathway. This is further confirmed through the FACS analyses (Fig. 5f). For this purpose, MDA-MB-231 cells were treated with the **1/β-CD$^+$/Hem/DNA1** nanosheet under NIR light illumination and analysed by flow cytometry after staining with Annexin V-FITC

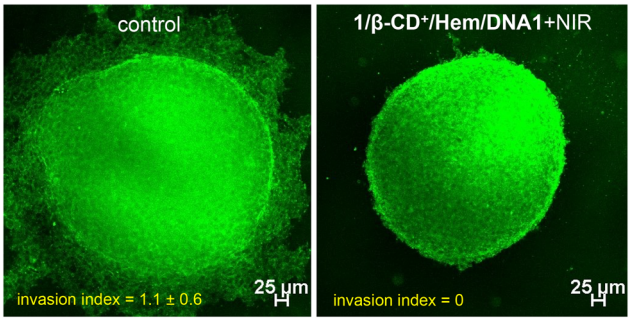

Fig. 6 CLSM images of **1/β-CD$^+$/Hem/DNA1**-treated MDA-MB-231 3D spheroids after NIR light illumination (0.75 W cm^{-2} for 10 minutes) (right) and the corresponding untreated control spheroids (left).

(AV)/PI. In accordance with the CLSM, the cell population mainly shifted to the quadrant corresponding to the apoptotic pathway. These results collectively reveal that the **1/β-CD$^+$/Hem/DNA1** nanosheet under NIR light illumination induces cell death *via* the oxidative stress-induced apoptotic pathway.

After demonstrating the *in vitro* performance of the **1/β-CD$^+$/Hem/DNA1** nanosheet, we studied the efficiency of the nanoformulation in the multicellular tumor spheroid model using a 3D cell culture (Fig. 6). The 3D-multicellular tumor spheroid mimics the *in vivo* tumor and undergoes proliferation in all directions similar to malignant tumors. In a 3D cell culture, cells clump together to form a stable 3D spheroid-like structure, wherein the communication and signalling between the cells are maximized, leading to efficient proliferation and invasion over time.[55] To this end, 3D tumour spheroids of MDA-MB-231 cells were prepared using the standard hanging drop method.[56,57] The invasion potential of the 3D spheroids was studied in the presence of the **1/β-CD$^+$/Hem/DNA1** nanosheet after NIR light irradiation to understand its effect on spheroid invasion. For this, 3D spheroids were incubated with **1/β-CD$^+$/Hem/DNA1** (20/20/1/1 μM) nanosheets for 4 h, kept under irradiation at 635 nm (0.75 W cm^{-2}) for 10 minutes followed by 24 h of incubation. Untreated spheroids were considered as controls that showed the maximum invasion potential (invasion index = 1.1 ± 0.6) as they showed migration in all directions. On the other hand, the **1/β-CD$^+$/Hem/DNA1**-treated sample showed a drastic reduction in the invasion potential (invasion index = 0) of the spheroids due to the combined therapeutic actions of CDT and PDT. These observations are in good agreement with the *in vitro* studies.

Conclusions

In summary, we have reported a supramolecular strategy for the fabrication of a PDT-active 2D nanosheet loaded with a POD-mimicking DNAzyme for the synergetic combination of PDT and CDT for targeted cancer therapy. The most important feature of the present nanoformulation is the synergetic combination of CDT and PDT actions. The CDT action of the nanoformulation results in the formation of highly toxic ROSs along with the generation of O_2 as one of the bioproducts, which can boost the concentration of O_2 in the tumour microenvironment. This in turn enhances the PDT action of the nanoformulation, which is otherwise found to be less effective due to tissue hypoxia. Excellent therapeutic activity was demonstrated both *in vitro* and *in vivo* for targeted cancer therapy. This work represents a unique combination of CDT and PDT for targeted cancer therapy, wherein the CDT action of the nanoagent enhances the PDT efficacy and we strongly believe that this approach will encourage researchers to design similar combination therapies for advancements in the treatment of cancer.

Author contributions

The manuscript was written through the contributions of all authors. All authors have given approval to the final version of the manuscript.

Data availability

The data supporting this article have been included as part of the ESI.†

Conflicts of interest

There are no conflicts to declare.

Acknowledgements

Financial support from the SERB (CRG/2022/002612) is gratefully acknowledged. Sarika Mohan. S is acknowledged for help with the FACS analyses.

References

1 X. Zhao, J. Liu, J. Fan, H. Chao and X. Peng, *Chem. Soc. Rev.*, 2021, **50**, 4185–4219.
2 T. C. Pham, V.-N. Nguyen, Y. Choi, S. Lee and J. Yoon, *Chem. Rev.*, 2021, **121**, 13454–13619.
3 S. S. Lucky, K. C. Soo and Y. Zhang, *Chem. Rev.*, 2015, **115**, 1990–2042.
4 K. Jibin, M. Victor, G. Saranya, H. Santhakumar, V. Murali, K. K. Maiti and R. S. Jayasree, *ACS Appl. Bio Mater.*, 2021, **4**, 5742–5752.
5 H. He, P.-C. Lo, S.-L. Yeung, W.-P. Fong and D. K. P. Ng, *J. Med. Chem.*, 2011, **54**, 3097–3102.
6 D. Perumal, M. Golla, K. S. Pillai, G. Raj, A. Krishna P. K. and R. Varghese, *Org. Biomol. Chem.*, 2021, **19**, 2804–2810.
7 Y. Wang, M. Feng, B. Lin, X. Peng, Z. Wang and R. Lv, *Nanoscale*, 2021, **13**, 18125–18133.

8 R. Lv, M. Raab, Y. Wang, J. Tian, J. Lin and P. N. Prasad, *Coord. Chem. Rev.*, 2022, **460**, 214486.
9 B. Li, D. Xu, Y. Chen, W. Li, H. Liu, A. A. Ansari and R. Lv, *ACS Appl. Nano Mater.*, 2024, **7**, 9428–9440.
10 L. Feng, L. Cheng, Z. Dong, D. Tao, T. E. Barnhart, W. Cai, M. Chen and Z. Liu, *ACS Nano*, 2017, **11**, 927–937.
11 X. Shi, H. Guo, X. Zhang, X. Zhang, C. Cao, H. Li, S. Chen, L. Han and S. Wang, *ACS Mater. Lett.*, 2023, **5**, 2332–2338.
12 H. Tian, Z. Luo, L. Liu, M. Zheng, Z. Chen, A. Ma, R. Liang, Z. Han, C. Lu and L. Cai, *Adv. Funct. Mater.*, 2017, **27**, 1703197.
13 C. McEwan, S. Kamila, J. Owen, H. Nesbitt, B. Callan, M. Borden, N. Nomikou, R. A. Hamoudi, M. A. Taylor, E. Stride, A. P. McHale and J. F. Callan, *Biomaterials*, 2016, **80**, 20–32.
14 R. Zhou, T. Y. Ohulchanskyy, H. Xu, R. Ziniuk and J. Qu, *Small*, 2021, **17**, 2103569.
15 H. Wang, Y. Xie, Y. Chen, H. Zhao, X. Lv, Z. Zhang, G. Li, J. Pan, J. Wang and Z. Liu, *Adv. Healthcare Mater.*, 2023, **12**, 2300848.
16 S. Wang, S. Tavakoli, R. P. Parvathaneni, G. N. Nawale, O. P. Oommen, J. Hilborn and O. P. Varghese, *Biomater. Sci.*, 2022, **10**, 6399–6412.
17 J. Xu, L. Xu, C. Wang, R. Yang, Q. Zhuang, X. Han, Z. Dong, W. Zhu, R. Peng and Z. Liu, *ACS Nano*, 2017, **11**, 4463–4474.
18 M. Overchuk, R. A. Weersink, B. C. Wilson and G. Zheng, *ACS Nano*, 2023, **17**, 7979–8003.
19 Z. Tang, Y. Liu, M. He and W. Bu, *Angew. Chem., Int. Ed.*, 2019, **58**, 946–956.
20 Y. Zhou, S. Fan, L. Feng, X. Huang and X. Chen, *Adv. Mater.*, 2021, **33**, 2104223.
21 Z. Yu, Y. Hu, Y. Sun and T. Sun, *Chem. – Eur. J.*, 2021, **27**, 13953–13960.
22 P. Zhao, H. Li and W. Bu, *Angew. Chem., Int. Ed.*, 2023, **62**, e202210415.
23 H. Hou, X. Huang, G. Wei, F. Xu, Y. Wang and S. Zhou, *ACS Appl. Mater. Interfaces*, 2019, **11**, 29579–29592.
24 J. Qin, B. Bo, T. Yang, Z. Wang, F. Xie and H. Peng, *Mater. Lett.*, 2023, **349**, 134678.
25 S. Shen, M. Liu, T. Li, S. Lin and R. Mo, *Biomater. Sci.*, 2017, **5**, 1367–1381.
26 K. Li, Y. Zhang, A. Hussain, Y. Weng and Y. Huang, *ACS Biomater. Sci. Eng.*, 2021, **7**, 4420–4429.
27 R. N. Woodring, E. G. Gurysh, E. M. Bachelder and K. M. Ainslie, *ACS Appl. Bio Mater.*, 2023, **6**, 934–950.
28 P. Liang, B. Ballou, X. Lv, W. Si, M. P. Bruchez, W. Huang and X. Dong, *Adv. Mater.*, 2021, **33**, 2005155.
29 G. Raj, Vasudev D. S., J. Prasad, E. Anbu, S. Ram, G. B. Daniel, N. D. Narendradev, S. M. Srinivasula and R. Varghese, *Mater. Chem. Front.*, 2024, **8**, 553–561.
30 A. Saminathan, J. Devany, A. T. Veetil, B. Suresh, K. S. Pillai, M. Schwake and Y. Krishnan, *Nat. Nanotechnol.*, 2021, **16**, 96–103.
31 K. Dutta, R. Das, J. Medeiros and S. Thayumanavan, *Biochemistry*, 2021, **60**, 966–990.
32 C. Liu, J. Hu, W. Yang, J. Shi, Y. Chen, X. Fan, W. Gao, L. Cheng, Q.-Y. Luo and M. Zhang, *Nanoscale*, 2024, **16**, 4637–4646.
33 P. Borah, D. J. Baruah, P. Mridha, R. Baishya, H. K. Borab and M. R. Das, *Chem. Commun.*, 2024, **60**, 2417–2420.
34 S. Liu, *et al.*, *Adv. Mater.*, 2024, **36**, 2304297.
35 X. Xie, Y. Wang, X. Zhou, J. Chen, M. Wang and X. Su, *Analyst*, 2021, **146**, 896–903.
36 Q. Zhang, Q. Jiang, N. Li, L. Dai, Q. Liu, L. Song, J. Wang, Y. Li, J. Tian, B. Ding and Y. Du, *ACS Nano*, 2014, **8**, 6633–6643.
37 P. Pitikultham, Z. Wang, Y. Wang, Y. Shang, Q. Jiang and B. Ding, *ChemMedChem*, 2022, **17**, e202100635.
38 S. Dey, A. Dorey, L. Abraham, Y. Xing, I. Zhang, F. Zhang, S. Howorka and H. Yan, *Nat. Commun.*, 2022, **13**, 2271.
39 Y. Cao, P. Ding, L. Yang, W. Li, Y. Luo, J. Wang and R. Pei, *Chem. Sci.*, 2020, **11**, 6896–6906.
40 L. Fabre, C. Rousset, K. Monier, F. Da Cruz-Boisson, P. Bouvet, M.-T. Charreyre, T. Delair, E. Fleury and A. Favier, *Biomacromolecules*, 2022, **23**, 2302–2314.
41 W. Xuan, Y. Xia, T. Li, L. Wang, Y. Liu and W. Tan, *J. Am. Chem. Soc.*, 2020, **142**, 937–944.
42 C. Zhang, S. Tang, M. Wang, L. Li, J. Li, D. Wang, X. Mi, Y. Zhang, X. Tan and S. Yue, *ACS Nano*, 2024, **18**, 5470–5482.
43 J. He, T. Peng, Y. Peng, L. Ai, Z. Deng, X.-Q. Wang and W. Tan, *J. Am. Chem. Soc.*, 2020, **142**, 2699–2703.
44 A. F.-J. Jou, Y.-T. Chou, I. Willner and J. A. Ho, *Angew. Chem., Int. Ed.*, 2021, **60**, 21673–21678.
45 W. Xuan, Y. Xia, T. Li, L. Wang, Y. Liu and W. Tan, *J. Am. Chem. Soc.*, 2020, **142**, 937–944.
46 S. K. Albert, H. V. P. Thelu, M. Golla, N. Krishnan and R. Varghese, *Nanoscale*, 2017, **9**, 5425–5432.
47 W. Tang and S.-C. Ng, *Nat. Protoc.*, 2008, **3**, 691–697.
48 A. Tamura, K. Nishida, S. Zhang, T. W. Kang, A. Tonegawa and N. Yui, *ACS Biomater. Sci. Eng.*, 2022, **8**, 2463–2476.
49 Y. Guo, J. Zhang, F. Ding, G. Pan, J. Li, J. Feng, X. Zhu and C. Zhang, *Adv. Mater.*, 2019, **31**, 1807533.
50 G. Raj, D. S. Vasudev, S. Christopher, A. Babulal, P. Harsha, S. Ram, M. Tiwari, M. Sauer and R. Varghese, *Nanoscale*, 2024, **16**, 3755–3763.
51 N. Neelambaran, S. Shamjith, V. P. Murali, K. K. Maiti and J. Joseph, *ACS Appl. Bio Mater.*, 2023, **6**, 5776–5788.
52 W. Li, S. Yin, Y. Shen, H. Li, L. Yuan and X.-B. Zhang, *J. Am. Chem. Soc.*, 2023, **145**, 3736–3747.
53 S.-H. Park, S. Park and I. Shin, *STAR Protoc.*, 2021, **2**, 100349.
54 W. E. M. Noteborn, S. K. Vittala, M. B. Torredemer, C. Maity, F. Versluis, R. Eelkema and R. E. Kieltyka, *Biomacromolecules*, 2023, **24**, 377–386.
55 A. Rajwar, S. R. Shetty, P. Vaswani, V. Morya, A. Barai, S. Sen, M. Sonawane and D. Bhatia, *ACS Nano*, 2022, **16**, 10496–10508.
56 H. A Naveena and D. Bhatia, *ChemBioChem*, 2023, e202300506.
57 A. Aung, S. K. Davey, J. Theprungsirikul, V. Kumar and S. Varghese, *Adv. Healthcare Mater.*, 2023, **12**, 2201842.